SUPPORTING INFORMATION

Feasibility of using bimetallic Au−Ag nanoparticles for organic light-emitting devices

Bei Liu,[†,∇] Mochamad Januar,[*,†,∇] Jui-Ching Cheng,[‡] Koji Hatanaka,[¶,§,‖] Hiroaki Misawa,[⊥,#] and Kou-Chen Liu[*,†,@,△]

†*Department of Electronic Engineering, Chang Gung University, Taoyuan 33302, Taiwan*
‡*Department of Electronic Engineering, National Taipei University of Technology, Taipei 10608, Taiwan*
¶*Research Center for Applied Sciences, Academia Sinica, Taipei 11529, Taiwan*
§*College of Engineering, Chang Gung University, Taoyuan 33302, Taiwan*
‖*Department of Materials Science and Engineering, National Dong Hwa University, Hualien 97401, Taiwan*
⊥*Research Institute for Electronic Science, Hokkaido University, Sapporo 001-0021, Japan*
#*Center for Emergent Functional Matter Science, National Chiao Tung University, Hsinchu 30010, Taiwan*
@*Division of Pediatric Infectious Disease, Department of Pediatrics, Chang Gung Memorial Hospital, Linkou 33305, Taiwan*
△*Department of Materials Engineering, Ming Chi University of Technology, New Taipei City 24301, Taiwan*
∇*These authors contributed equally to this work*

E-mail: d0727105@cgu.edu.tw; jacobliu@mail.cgu.edu.tw
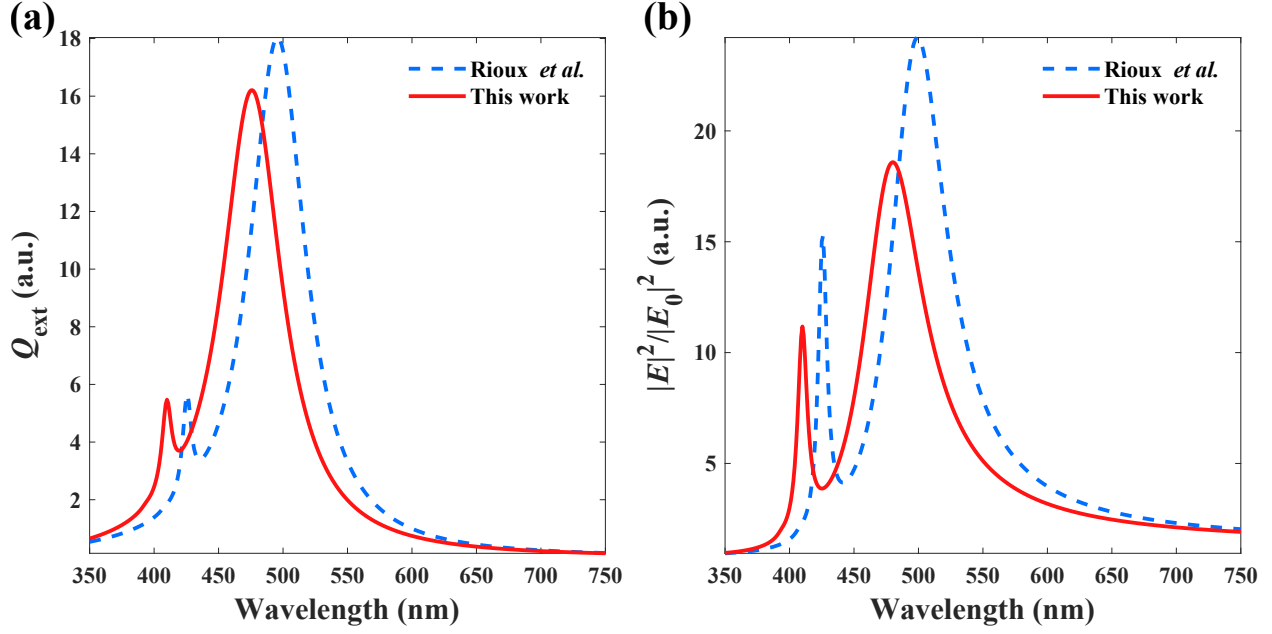Phone: +886-3-211-8800 (ext. 3152). Fax: +886-3-211-8507

Figure S1: Comparison of (a) extinction efficiency and (b) electric-field intensity for a single Ag nanoparticle with a diameter of 50 nm calculated based on the original (Rioux *et al.*[1]) and refined (Johnson and Christy[2]) dielectric functions.
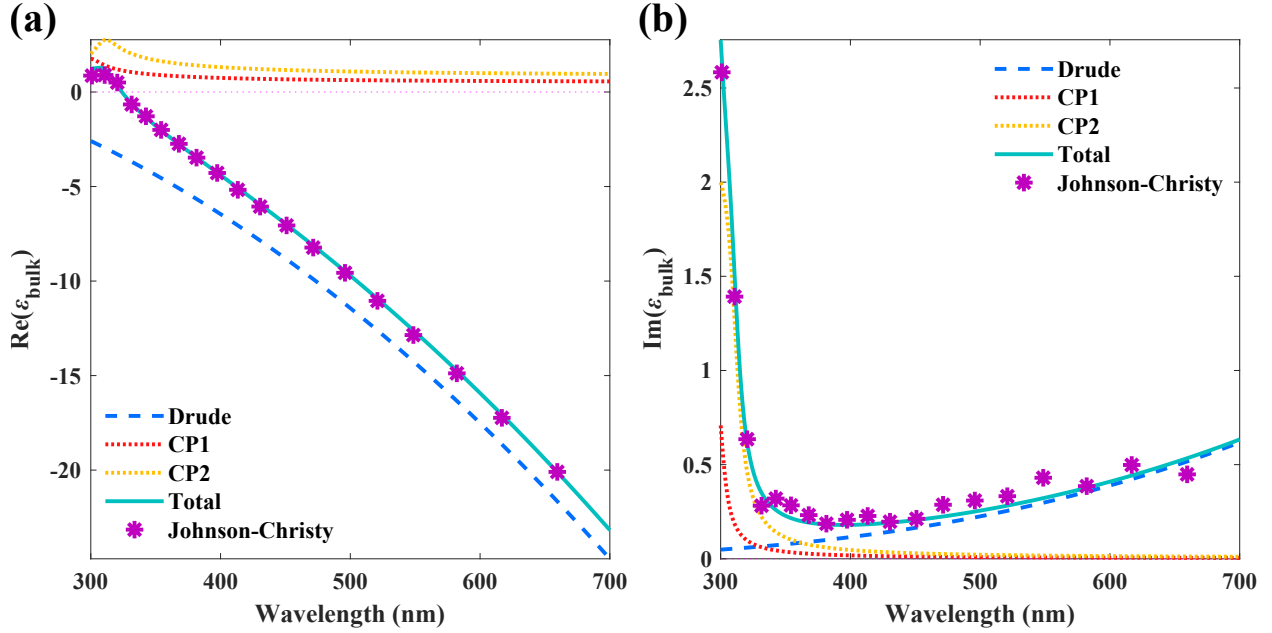

Figure S2: Fitting of the (a) real and (b) imaginary components of the bulk dielectric function of Ag. The Johnson and Christy databases are also shown for reference (scatter dot).

Alloy Dielectric Functions

Figure S1 displays the discrepancies arising in the extinction spectrum and the near-field intensity for the pure Ag reference calculated based on the dielectric functions from Rioux

et al.[1] and Johnson and Christy.[2]

We used the parabolic relationship in Eq. 3 of the main text to simulate Au_xAg_{1-x} alloy NPs for arbitrary compositions. In this case, three-point reference parameters are required, *e.g.*, pure Au, $Au_{0.5}Ag_{0.5}$, and pure Ag. These parameters were taken based on the work of Rioux *et al.*,[1] except for pure Ag. The pure Ag reference is refitted based on Johnson and Christy's[2] experimental data to provide more reliable results. Figure S2 shows the fitting result for the Ag monometallic dielectric function, calculated using Eqs. 1 and 2 of the main text.

Below, we provided the best-fitted parabolic equations as a function of the molar fraction of Au (x) based on Eq. 3 of the main text.

$$
\begin{aligned}
\varepsilon_\infty(x) &= 0.1798x^2 - 0.2943x + 2.3860 \;, \\
\omega_p(x) &= 0.1976x^2 - 0.4932x + 9.2190 && \text{[eV]}, \\
\omega_{g1}(x) &= 1.5618x^2 - 3.0541x + 4.1575 && \text{[eV]}, \\
\omega_{01}(x) &= 1.7930x^2 - 3.4933x + 4.0960 && \text{[eV]}, \\
\omega_{02}(x) &= 1.6824x^2 - 2.1312x + 3.9850 && \text{[eV]}, \\
\Gamma_p(x) &= -0.50289x^2 + 0.50485x + 0.04043 && \text{[eV]}, \\
\Gamma_1(x) &= -0.26126x^2 + 0.37283x + 0.06723 && \text{[eV]}, \\
\Gamma_2(x) &= -1.85264x^2 + 2.12212x + 0.08519 && \text{[eV]}, \\
A_1(x) &= 194.952x^2 - 191.918x + 70.217 \;, \\
A_2(x) &= -95.606x^2 + 108.343x + 27.270 \;.
\end{aligned}
\tag{S1}
$$

Figure S3 shows the behavior of these parabolic equations. This figure remarks the following key points.

- The plasma frequency ω_p varies only up to ~ 0.296 eV across all compositions, verifying that the densities of valence electrons for the two metals and their alloys are nearly identical.
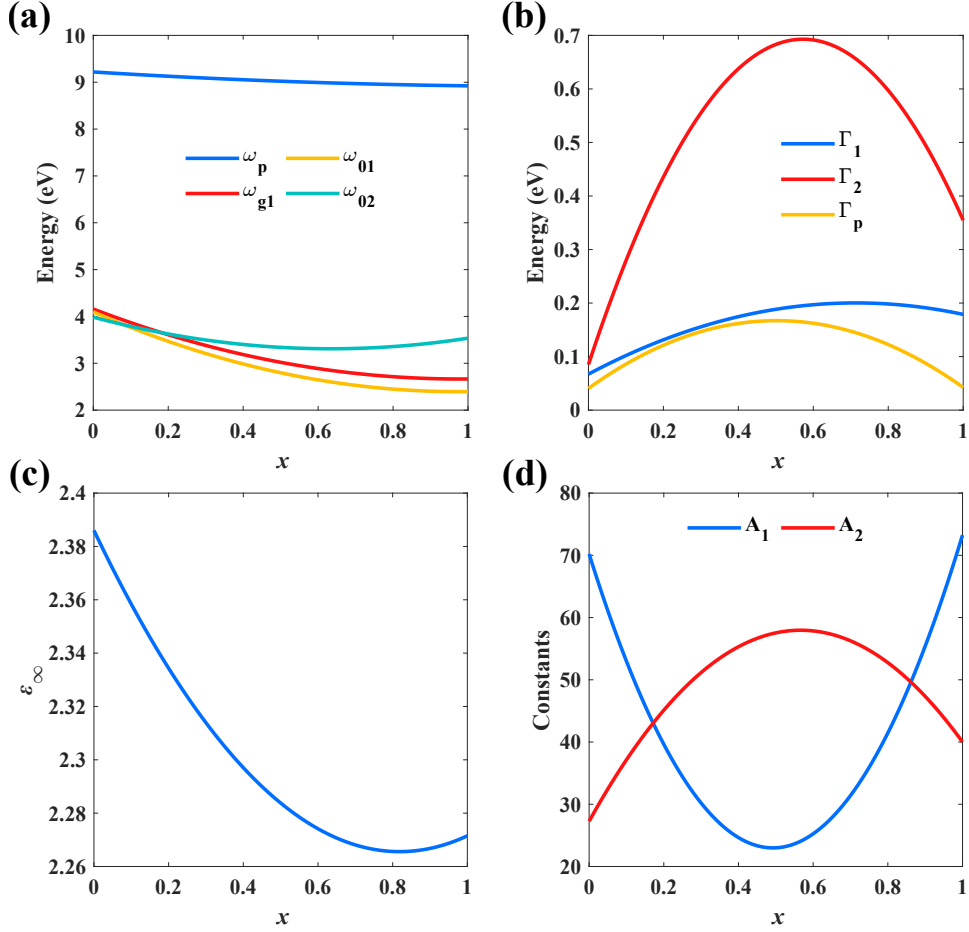
Figure S3: Evolution of (a) the frequency parameters (ω_p, ω_{g1}, ω_{01}, and ω_{02}), (b) the broadening factors (Γ_1, Γ_2, and Γ_p), (c) the contribution from high-energy transitions (ε_∞), and (d) the amplitude parameters (A_1 and A_2) as a function of the molar fraction of Au (x).

- $\omega_p = 9.219$ eV for Ag. This value is very similar to that obtained by another group[3] who also extracted parameters from the Johnson-Christy dataset.

- Both ω_{01} and ω_{g1} parameters still retain the same behavior as those in Ref. 1, suggesting that the band separation varies monotonically with the alloy composition.

- A smaller variation (~ 0.449 eV) is observed for ω_{02}, which is a consequence of the comparable band separations in Au and Ag at the L symmetry point.[1]

- The broadening factors (Γ_p, Γ_1, and Γ_2) are higher in alloys than in pure Au and Ag. This trend is consistent given that alloys are likely disordered materials. Mixed
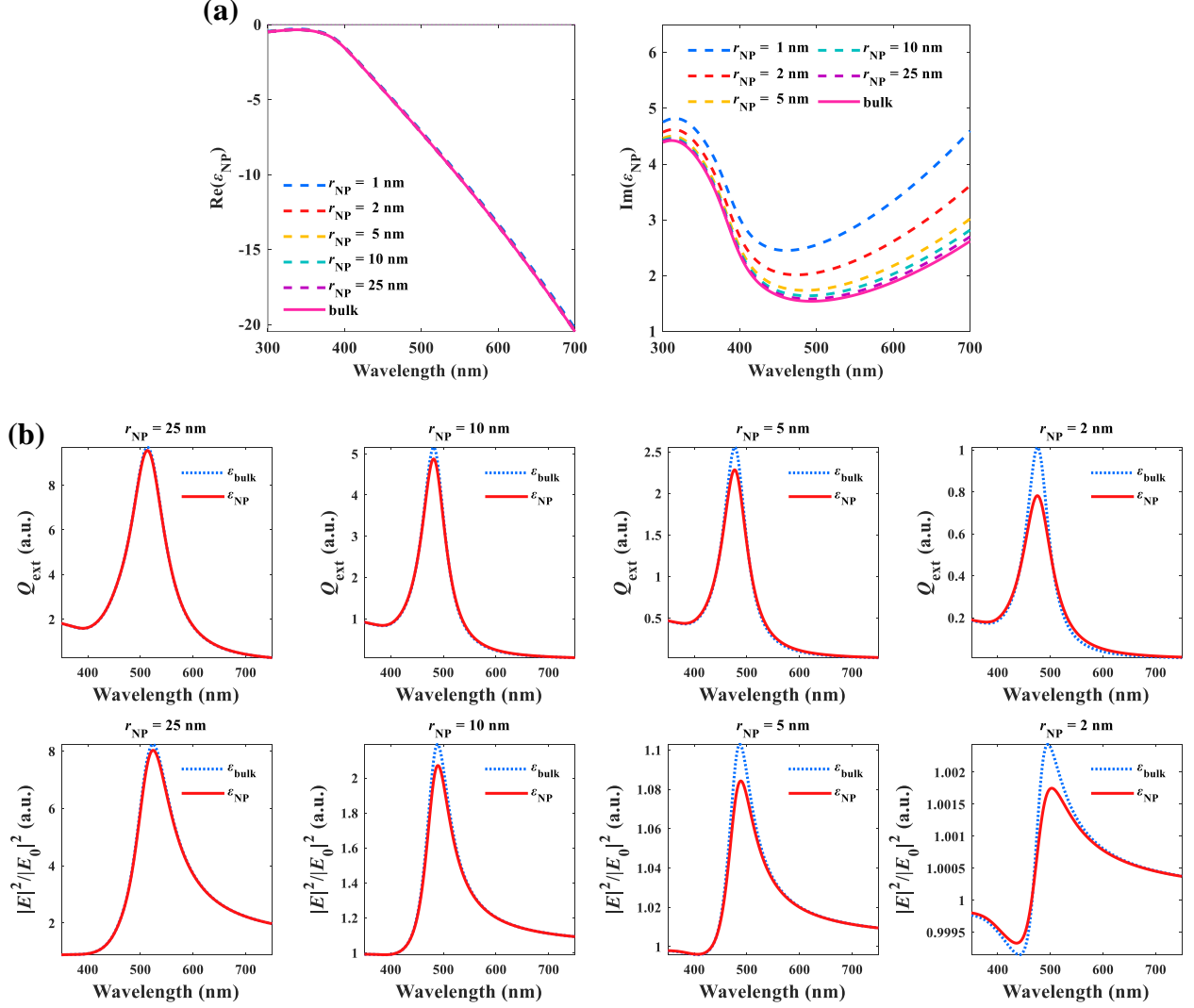
Figure S4: (a) Real and imaginary parts of the dielectric function of the $Au_{0.36}Ag_{0.64}$ alloy for different nanoparticle radii (r_{NP}). (b) Extinction spectrum (upper panels) and the orientationally averaged electric-field intensity (lower panels) calculated from the bulk (ε_{bulk}) and the corrected (ε_{NP}) dielectric permittivities of $Au_{0.36}Ag_{0.64}$ alloy NPs at various r_{NP}.

Au and Ag atoms create a random distribution in the crystal lattice that destroys the periodicity of the structure.

Figures S4(a) and (b) show the impact of size correction on the dielectric function of the alloy nanoparticles and the far-field and near-field spectra at various nanoparticle radii. In the calculations, the molar fraction of Au was set to be 0.36.

Spherical Vectorial Functions

Below, we provide the explicit expressions for the spherical vectorial functions $\mathbf{M}_{o1\ell}$ and $\mathbf{N}_{e1\ell}$ corresponding to Eq. 7 of the main text, as follows [4]

$$
\begin{aligned}
\mathbf{M}_{o1\ell}^{(1)} &= \frac{\psi_\ell\,(kr)}{kr} \left(\frac{P_\ell^1(\cos\theta)}{\sin\theta} \cos\varphi\,\hat{\mathbf{e}}_\theta - \frac{\partial P_\ell^1(\cos\theta)}{\partial\theta} \sin\varphi\,\hat{\mathbf{e}}_\varphi \right)\,, \\
\mathbf{M}_{o1\ell}^{(3)} &= \frac{\xi_\ell\,(kr)}{kr} \left(\frac{P_\ell^1(\cos\theta)}{\sin\theta} \cos\varphi\,\hat{\mathbf{e}}_\theta - \frac{\partial P_\ell^1(\cos\theta)}{\partial\theta} \sin\varphi\,\hat{\mathbf{e}}_\varphi \right)\,, \\
\mathbf{N}_{e1\ell}^{(1)} &= \ell(\ell+1)\frac{\psi_\ell\,(kr)}{(kr)^2} P_\ell^1(\cos\theta)\cos\varphi\,\hat{\mathbf{e}}_r \\
&\quad + \frac{\psi_\ell'\,(kr)}{kr} \left(\frac{\partial P_n^1(\cos\theta)}{\partial\theta} \cos\varphi\,\hat{\mathbf{e}}_\theta - \frac{P_\ell^1(\cos\theta)}{\sin\theta} \sin\varphi\,\hat{\mathbf{e}}_\varphi \right)\,, \\
\mathbf{N}_{e1\ell}^{(3)} &= \ell(\ell+1)\frac{\xi_\ell\,(kr)}{(kr)^2} P_\ell^1(\cos\theta)\cos\varphi\,\hat{\mathbf{e}}_r \\
&\quad + \frac{\xi_\ell'\,(kr)}{kr} \left(\frac{\partial P_n^1(\cos\theta)}{\partial\theta} \cos\varphi\,\hat{\mathbf{e}}_\theta - \frac{P_\ell^1(\cos\theta)}{\sin\theta} \sin\varphi\,\hat{\mathbf{e}}_\varphi \right)\,.
\end{aligned}
\tag{S2}
$$

where $k = 2\pi n_{\text{host}}/\lambda$ is the wave number, n_{host} is the refractive index of the host medium, λ is the incident wavelength, $P_\ell^1(\cos\theta)$ is the associated Legendre function, $r = |\mathbf{r}|$ is the length of the radius vector $\mathbf{r}$ from the nanoparticle center to a point of interest, $0 \leq \theta \leq \pi$ and $0 \leq \varphi \leq 2\pi$ are spherical angles, and $\hat{\mathbf{e}}_r$, $\hat{\mathbf{e}}_\theta$, and $\hat{\mathbf{e}}_\varphi$ are unit vectors of the spherical coordinate system. Additionally, the Ricatti-Bessel functions ψ and ξ are defined as

$$
\begin{aligned}
\psi(kr) &= krj_\ell(kr)\,, \\
\xi(kr) &= krh_\ell^{(1)}(kr)\,,
\end{aligned}
\tag{S3}
$$

with j_ℓ and $h_\ell^{(1)}$, respectively, are the spherical Bessel functions of the first and third kind (Hankel function), and the prime notation denotes the first-order derivative with respect to the argument in parentheses.
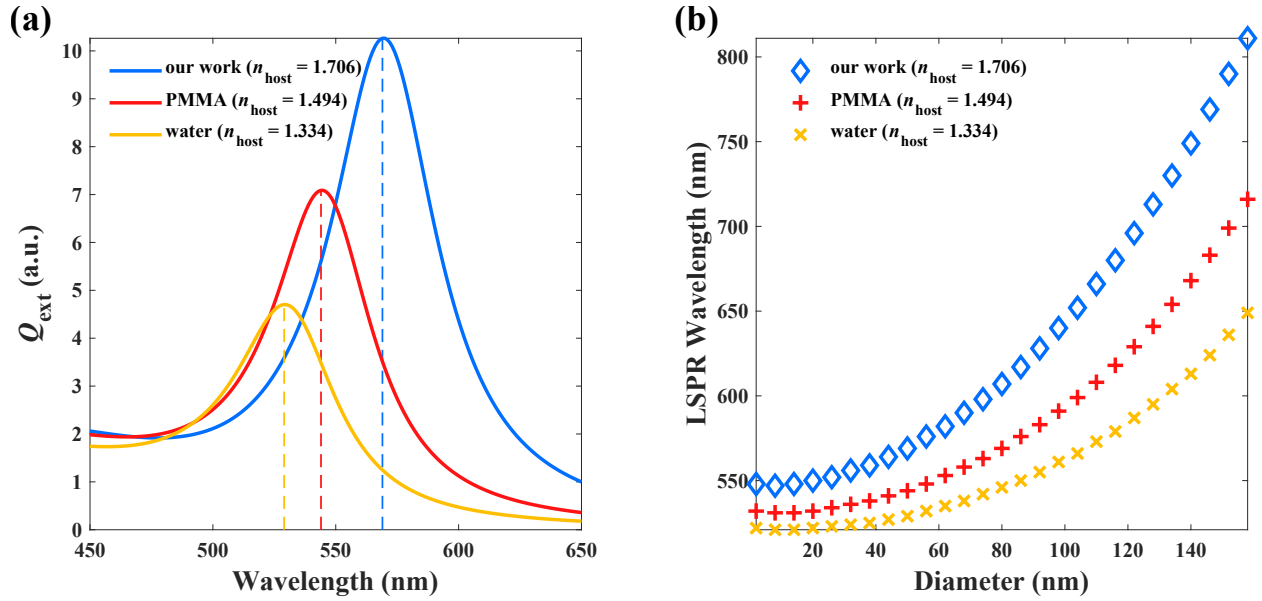
Figure S5: (a) Extinction efficiency for gold nanoparticles with a diameter of 50 nm with variations in the refractive index of the host medium. (b) Evolution of the peak wavelength of the extinction spectrum as a function of the diameter of the nanoparticles in the different host media.

Extinction Efficiencies in Different Host Media

Figure S5(a) shows the extinction spectrum for the pure Au nanoparticle (Au_xAg_{1-x} with $x = 1$) with a diameter of 50 nm embedded in different host media calculated using Eqs. 5 and 6 of the main text. In an aqueous solution, the peak of the extinction spectrum is centered at 529 nm. Owing to their higher refractive indices, the LSPR spectrum shifts to 544 nm and 569 nm when poly(methyl methacrylate) (PMMA) and OLED polymers are used as the host medium, respectively. These calculated LSPR wavelengths are consistent with previously reported experimental results.[5–7] Correspondingly, the evolution of the dipolar-LSPR wavelength as a function of the diameter of the nanoparticles also shifts towards longer wavelengths as the refractive index of medium increases (see Fig. S5(b)).

Quantum Yield

The expression for quantum yield can be deduced by considering the intrinsic quantum yield of the isolated molecule defined as

$$Q^0 = \frac{\gamma_{\text{rad}}^0}{\gamma_{\text{rad}}^0 + \gamma_{\text{nrad}}^0} \ . \tag{S4}$$

with γ_{rad}^0 and γ_{nrad}^0 are the intrinsic radiative and nonradiative decay rates, respectively. In the presence of a nanoparticle, the quantum yield is modified to

$$Q = \frac{\gamma_{\text{rad}}}{\gamma_{\text{rad}} + \gamma_{\text{nrad}}^0 + \gamma_{\text{loss}}} \tag{S5}$$

due to the strong enhancement in the radiative decay rate, such that $\gamma_{\text{rad}} \geq \gamma_{\text{rad}}^0$, and an additional nonradiative decay channel, γ_{loss}. Here, we assumed that the intrinsic nonradiative decay of the molecule is not affected by the metal, such that $\gamma_{\text{nrad}} = \gamma_{\text{nrad}}^0$. By combining Eqs. S4 and S5, we arrive at the usual expression for the quantum yield as[8]

$$Q = \frac{\gamma_{\text{rad}}/\gamma_{\text{rad}}^0}{\gamma_{\text{rad}}/\gamma_{\text{rad}}^0 + \gamma_{\text{loss}}/\gamma_{\text{rad}}^0 + (1 - Q^0)/Q^0} \ . \tag{S6}$$

However, to clearly evaluate the influence of the intrinsic properties of the emissive materials (Q^0), we can modify Eq. S6 as follows

$$\frac{Q}{Q^0} = \frac{1}{Q^0} \frac{\gamma_{\text{rad}}/\gamma_{\text{rad}}^0}{\gamma_{\text{tot}}/\gamma_{\text{rad}}^0 + (1 - Q^0)/Q^0} \ . \tag{S7}$$

Here, the equation was divided by Q^0, and the sum of the radiative and non-radiative decay rates was condensed into one variable: $\gamma_{\text{tot}} \equiv \gamma_{\text{rad}} + \gamma_{\text{loss}}$. After some reordering, we have

$$\frac{Q}{Q^0} = \frac{\gamma_{\text{rad}}/\gamma_{\text{rad}}^0}{1 + Q^0 \left(\gamma_{\text{tot}}/\gamma_{\text{rad}}^0 - 1 \right)} \ . \tag{S8}$$
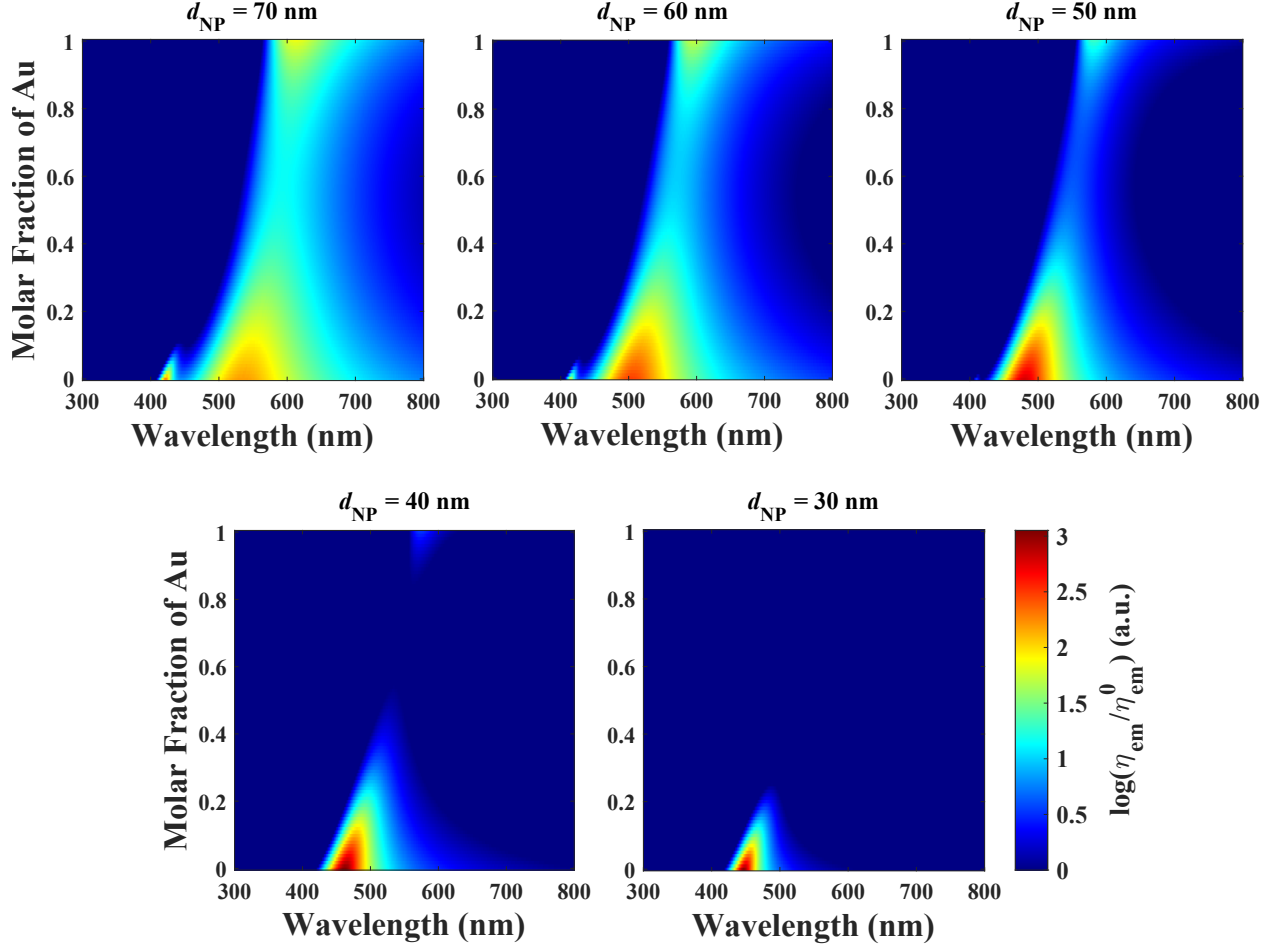
Figure S6: Mapping of the luminescent efficiency as a function of wavelength and molar fraction of Au for different nanoparticle diameters (d_{NP}).

This is Eq. 13 from the main text.

Luminescence Enhancement Mapping

Figure S6 shows the mappings of the luminescent efficiency of the $\mathrm{Au}_x\mathrm{Ag}_{1-x}$ nanoparticles for different diameters. In the figure, the region with maximum efficiency (red spot) becomes more intense as the size of the nanoparticles is reduced, suggesting that the smaller nanoparticle has the potential to produce higher luminescent efficiency than the larger one. However, the adjustable window for wavelength and alloy composition, which enhances luminescence by more than one order ($\log\left(\eta_{\mathrm{em}}/\eta_{\mathrm{em}}^0\right) > 1$), becomes narrower in the smaller nanoparticles.
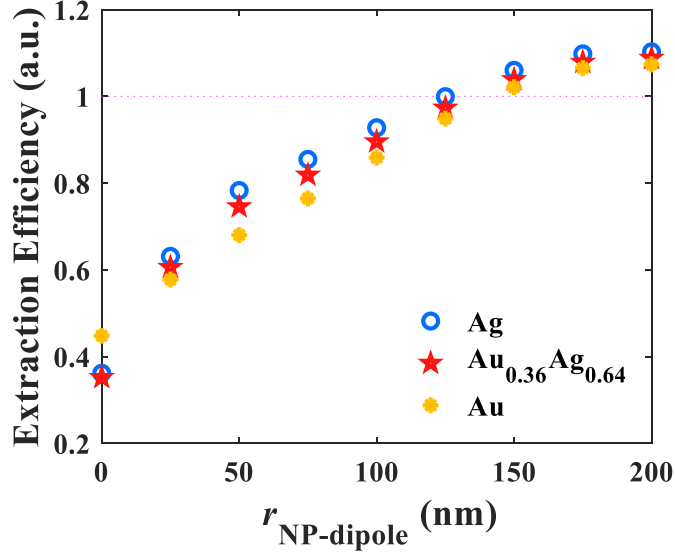
Figure S7: The light-extraction efficiency as a function of nanoparticle-dipole distance.

For instance, at $d_{\mathrm{NP}} = 30$ nm, the values of $\log\left(\eta_{\mathrm{em}}/\eta_{\mathrm{em}}^0\right) > 1$ are only observed at wavelengths between $\sim$430 nm and $\sim$480 nm, and the adjustability of the Au molar fraction is limited to $x \lesssim 0.2$. In contrast, although there is a slight decrease in the maximum efficiency, the window for obtaining enhanced luminescence is wider when using the larger nanoparticles. As indicated by the 70-nm-diameter nanoparticle, the values of $\log\left(\eta_{\mathrm{em}}/\eta_{\mathrm{em}}^0\right) > 1$ extend to longer wavelengths up to $\sim$700 nm, and the compositional adjustment applies to more extensive x-values ranging from 0 to 1. Therefore, the larger nanoparticles offer more options for tuning the Au$-$Ag compositions to enhance luminescent efficiency over a broader working wavelength.

Light-Extraction Efficiencies

Figure S7 shows the far-field emissions of a stacked structure calculated using the finite-difference time-domain (FDTD) method with varying dipole positions. For each point in the plot, six separate simulations were performed and averaged incoherently. In this case, two simulations were carried out to account for the dipole positions on the left and right sides of the nanoparticles, and each simulation was calculated individually in the dipolar

orientations of p_x, p_y, and p_z.

References

(1) Rioux, D.; Vallières, S.; Besner, S.; Muñoz, P.; Mazur, E.; Meunier, M. An Analytic Model for the Dielectric Function of Au, Ag, and their Alloys. *Advanced Optical Materials* **2014**, *2*, 176–182.

(2) Johnson, P. B.; Christy, R. W. Optical Constants of the Noble Metals. *Phys. Rev. B* **1972**, *6*, 4370–4379.

(3) McMahon, J. M.; Schatz, G. C.; Gray, S. K. Plasmonics in the ultraviolet with the poor metals Al, Ga, In, Sn, Tl, Pb, and Bi. *Phys. Chem. Chem. Phys.* **2013**, *15*, 5415–5423.

(4) Bohren, C. F.; Huffman, D. R. *Absorption and Scattering of Light by Small Particles*; Wiley, 1983; p 530.

(5) Kim, J.; Dantelle, G.; Revaux, A.; Berard, M.; Huignard, A.; Gacoin, T.; Boilot, J.-P. Plasmon-Induced Modification of Fluorescent Thin Film Emission Nearby Gold Nanoparticle Monolayers. *Langmuir* **2010**, *26*, 8842–8849, PMID: 20230040.

(6) Cho, C.; Kang, H.; Baek, S.-W.; Kim, T.; Lee, C.; Kim, B. J.; Lee, J.-Y. Improved Internal Quantum Efficiency and Light-Extraction Efficiency of Organic Light-Emitting Diodes via Synergistic Doping with Au and Ag Nanoparticles. *ACS Applied Materials & Interfaces* **2016**, *8*, 27911–27919, PMID: 27669058.

(7) Chen, C.-W.; Hsiao, S.-Y.; Chen, C.-Y.; Kang, H.-W.; Huang, Z.-Y.; Lin, H.-W. Optical properties of organometal halide perovskite thin films and general device structure design rules for perovskite single and tandem solar cells. *J. Mater. Chem. A* **2015**, *3*, 9152–9159.

(8) Bharadwaj, P.; Novotny, L. Spectral dependence of single molecule fluorescence enhancement. *Opt. Express* **2007**, *15*, 14266–14274.